Available online at www.sciencedirect.com
ScienceDirect
International Journal of Mass Spectrometry 271 (2008) 68–75
International Journal of Mass Spectrometry
www.elsevier.com/locate/ijms

Electron-impact ionization of atomic ions in the Sn and Xe isonuclear sequences

S.D. Loch [a,*], M.S. Pindzola [a], D.C. Griffin [b]

[a] *Department of Physics, Auburn University, Auburn, AL 36849, United States*
[b] *Department of Physics, Rollins College, Winter Park, FL 32789, United States*

Received 30 August 2007; received in revised form 25 September 2007; accepted 26 September 2007
Available online 2 October 2007

Abstract

Electron-impact ionization cross-sections for all atomic ions in the Sn and Xe isonuclear sequences are calculated using a semi-relativistic configuration-average distorted-wave method. Contributions to the cross-sections are included from both direct ionization and indirect excitation-autoionization. Branching ratio calculations are carried out for Cu-like $Sn^{21+}$and Xe^{25+} and Na-like Sn^{39+} and Xe^{43+} to determine when best to ignore indirect excitation-autoionization contributions due to radiation damping along the isonuclear sequences. Although experiments exist for Xe through to Xe^{6+}, Xe^{8+}, and Xe^{43+} the configuration-average distorted-wave results only agree well with the Xe^{8+} measurements, once metastable states are taken into account and with the Xe^{43+} measurements once radiation damping of the excitation-autoionization contribution is accounted for. Temperature-dependent rate coefficients are calculated for each Sn and Xe ionization stage and then put in a collisional-radiative format that should prove useful in modelling astrophysical and laboratory plasmas.
Published by Elsevier B.V.

Keywords: Ionization; Sn; Xe

1. Introduction

Accurate electron-impact ionization cross-sections and rate coefficients for atomic ions along isonuclear sequences are important for the fields of magnetic and inertial fusion energy, astrophysics, atmospheric physics, and the development of UV and X-ray light sources. In particular, both Sn and Xe are being explored as potential EUV radiators for the next generation of semiconductor devices [1,2].

Over the years, compilations of electron-impact ionization rates, generally based on perturbative distorted-wave calculations, have been made for many light and medium elements [3–5]. Recently, non-perturbative time-dependent close-coupling and R-matrix with pseudostates calculations have been carried out for electron-impact ionization cross-sections, temperature-dependent rate coefficients, and temperature and density-dependent generalized collisional-radiative coefficients for all atomic ions in the Li [6] and Be [7] isonuclear sequences. In addition, configuration-average distorted-wave calculations have also been carried out for selected heavy element isonuclear sequences, including Kr [8] and W [9].

In this paper we carry out configuration-average distorted-wave (CADW) calculations and report ionization cross-sections and temperature-dependent rate coefficients for all atomic ions in the Sn and Xe isonuclear sequences. To our knowledge, there are no electron ionization measurements on Sn atomic ions, although work is in progress[1]. There have been measurements of the neutral Sn ionization cross-section [10]. On the theory side there have been plane-wave Born calculations for the Sn neutral ion stage by McGuire [11]. On the other hand, electron-impact ionization cross-sections have been measured for the neutral Xe atom [12], Xe^{+}[13–15], $Xe^{q+}(q = 1 - 4)$ [16], Xe^{2+}[17], Xe^{3+}[18], Xe^{6+}[19], Xe^{8+}[20,21] and Xe^{43+}[22]. Theoretical calculations have been performed on Xe^{+}through to Xe^{6+}using a configuration-average distorted-wave method for the direct ionization and a term-resolved distorted-wave

* Corresponding author.
E-mail address: loch@physics.auburn.edu (S.D. Loch).

[1] A. Müller, private communication.

1387-3806/$ – see front matter. Published by Elsevier B.V.
doi:10.1016/j.ijms.2007.09.016

method for the excitation cross-sections [23,24]. Plane-wave Born calculations for neutral Xe were done by McGuire [11].

The work presented here is a survey of all Sn and Xe ions, the configuration-average distorted-wave is expected to be of reasonable quality, especially for the higher ion stages. There will, however, be ion stages for which the configuration-average distorted-wave approach is not sufficient. These ion stages will be identified with a view to improving the atomic data available for them in future work. In Section 2 we give a brief review of the configuration-average distorted-wave theory, in Section 3 we present selected cross-section and rate coefficient results along the Sn and Xe isonuclear sequences, while in Section 4 we conclude with a brief summary.

2. Configuration-average distorted-wave theory

In the independent processes approximation the total ionization cross-section is given by:

$$\sigma_{\rm ion} = \sigma_{\rm dion} + \sum_j \sigma^j_{\rm exc} B^{\rm a}_j, \tag{1}$$

where $\sigma_{\rm dion}$ is the direct ionization cross-section and $\sigma^j_{\rm exc}$ is the excitation cross-section to an autoionizing configuration j. The branching ratio for autoionization is given by:

$$B^{\rm a}_j = \frac{\sum_m A_{\rm a}(j \to m)}{\sum_m A_{\rm a}(j \to m) + \sum_n A_{\rm r}(j \to n)}, \tag{2}$$

where $A_{\rm a}$ is an autoionization rate and $A_{\rm r}$ is a radiative rate. We neglect the resonant capture followed by sequential double autoionization process since it is generally a small fraction of the total ionization cross-section and is confined to a small energy range below the upper excitation-autoionization thresholds.

Configuration-average expressions have been derived [25] for all the cross-sections and rates appearing in Eqs. (1) and (2). For direct ionization, a general transition between configurations has the form: $(nl)^w k_{\rm i} l_{\rm i} \to (nl)^{w-1} k_{\rm e} l_{\rm e} k_{\rm f} l_{\rm f}$, and the ionization cross-section is given by:

$$\sigma_{\rm dion} = \int_0^{E/2} d\epsilon_{\rm e} \frac{32w}{k_{\rm i}^3 k_{\rm e} k_{\rm f}} \sum_{l_{\rm i}, l_{\rm e}, l_{\rm f}} (2l_{\rm i}+1) \times (2l_{\rm e}+1)(2l_{\rm f}+1) |M(nl, k_{\rm i} l_{\rm i} \to k_{\rm e} l_{\rm e}, k_{\rm f} l_{\rm f})|^2, \tag{3}$$

where w is a subshell occupation number, nl are quantum numbers of the bound electron, $k_{\rm i} l_{\rm i}$, $k_{\rm e} l_{\rm e}$, and $k_{\rm f} l_{\rm f}$ are quantum numbers of the initial, ejected, and final continuum electrons, and the scattering matrix M is a sum over products of standard angular factors and radial direct and exchange electrostatic integrals. For electron-impact excitation to autoionizing configurations, a general transition between configurations has the form: $(n_1 l_1)^{w_1+1} (n_2 l_2)^{w_2-1} k_{\rm i} l_{\rm i} \to (n_1 l_1)^{w_1} (n_2 l_2)^{w_2} k_{\rm f} l_{\rm f}$, and the excitation cross-section is given by:

$$\sigma_{\rm exc} = \frac{8\pi}{k_{\rm i}^3 k_{\rm f}} (w_1+1)(4l_2+3-w_2) \sum_{l_{\rm i}, l_{\rm f}} (2l_{\rm i}+1) \times (2l_{\rm f}+1) |M(n_1 l_1, k_{\rm i} l_{\rm i} \to n_2 l_2, k_{\rm f} l_{\rm f})|^2, \tag{4}$$

where $n_1 l_1$ and $n_2 l_2$ are quantum numbers of the bound electrons, and $k_{\rm i} l_{\rm i}$ and $k_{\rm f} l_{\rm f}$ are quantum numbers of the initial and final continuum electrons. The energies and bound orbitals needed to evaluate all the configuration-average cross-sections and rates appearing in Eqs. (1) and (2) are calculated in the Hartree–Fock relativistic (HFR) approximation [26], which includes the mass–velocity and Darwin corrections with modified HF differential equations. The continuum radial orbitals, with normalization chosen as one times a sine function, are obtained by solving a single-channel radial Schrodinger equation, which also includes the mass–velocity and Darwin corrections, where the distorting potential is constructed from HFR bound orbitals. The configuration-average distorted-wave direct ionization cross-sections were evaluated such that the incident, scattered and ejected electrons were all calculated in a V^N potential (where N is the number of electrons on the initial target). For ion stages more than a few times ionized this is not expected to produce significantly different results from the other commonly used scattering potential (where the incoming and scattered electrons are calculated in a V^N potential while the ejected electron is calculated in a V^{N-1} potential). The scattering potential used here avoids the possibility of nonphysical shape resonances sometimes seen for neutral systems with the other potential [27].

3. Results

We used the configuration-average distorted-wave codes to calculate the direct and indirect ionization cross-sections. For select ion stages, configuration-average autoionizing branching ratios were calculated to determine when the radiative rates from the autoionizing configurations becomes competitive with the Auger rates.

When choosing which ionization channels to include in our configuration-average distorted-wave calculations we used the following guidelines. For the direct ionization all subshells that had an ionization potential above the single ionization threshold were used, including some that may lead to a double ionization. Thus, we included certain direct ionizations whose ionization potential lay above the double ionization potential. These were cases where the direct ionization cross-section from these subshells was large. One would need to track the Auger cascades to know how much of these processes produce single ionization and how much leads to double ionization. For example, we include the 5s, 4d, 4p, and 4s subshells in the direct ionization of Xe^{6+}. Ionization of the 5s and the 4d subshells leads to Xe^{7+}, ionization of the 4p and 4s subshells leads to Xe^{8+}, and ionization of the 3d subshell leads to either Xe^{8+}or Xe^{9+}[28]. We do not track such cascading processes in our calculations, considering it better to include such double ionization processes as a

single ionization than omitting these large cross-sections from the data that will be used in plasma modelling codes. At present most tokamak and astrophysics modelling codes do not track multiple ionizations, considering only single ionization jumps. The approach taken above is expected to be the most appropriate for application in current modelling codes. Thus, all of the cross-section plots shown here show only the single ionization contributions, for comparison with experiment, while the rate coefficients we archive include channels that can potentially lead to double ionization.

Similar guidelines were used when deciding which indirect processes to include. We calculated excitation cross-sections for inner subshell promotions to excited subshells up to 8f. All excitations to autoionizing configurations that lie above the single ionization potential are included. Certain strong excitation channels that lay above the double ionization threshold were also included. All of the ionization channels are shown in Tables 1 and 2, with the channels lying above the double ionization potential shown with the ∗ and † symbols.

3.1. Xe ionization

Results are shown for a selection of Xe ion stages in Figs. 1–3 . For the low ion stages the Auger rates are much greater than the radiative rates and the autoionizing levels will have branching ratios of one. Several of the low ion stages have autoionizing configurations with levels that straddle the ionization threshold. In the configuration-average method the levels of an autoionizing configuration will all be counted or will all be omitted, depending upon its configuration-average energy. For ion stages Xe^{+}through to Xe^{6+} it has already been shown [23,24] that the excitation-autoionization contributions are large. Griffin et al. [23] found that the structure of the autoionizing configuration resulting from a 4d electron being excited into the 4f subshell showed strong term-dependent effects. The term resolved excitation cross-sections were sensitive to these differences in the structure and wave functions. The effects were found to be small for Xe^{+} but were sizeable for Xe^{2+} through to Xe^{6+}, making a significant difference to the excitation-autoionization contribution to the ionization cross-section. Griffin et al. [23] also found that direct ionization of a 4d electron for Xe^{4+} leads to a configuration whose levels straddled the double ionization threshold, with only two thirds of these levels lying below the double ionization potential. Thus, for ion stages below Xe^{7+} the data of Griffin et al. [23] will be of higher quality than the configuration-average distorted-wave data presented here and is to be preferred.

Measurements for Xe^{8+}[20,21] are shown in Fig. 1. There is measured cross-section below the ground state ionization poten-

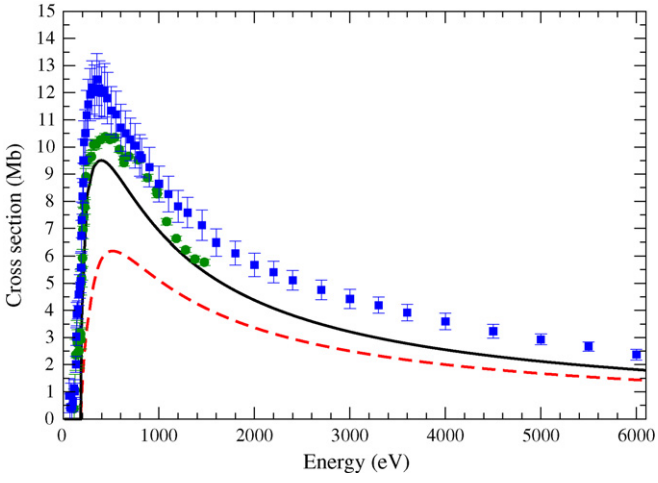

Fig. 1. Electron impact single ionization cross-section for Xe^{8+}. The dashed line shows the total direct ionization cross-section, the solid line shows the total direct ionization plus excitation-autoionization cross-sections. The squares show the experimental measurement of Stenke et al. [21] and the circles show the measurements of Bannister et al. [20].

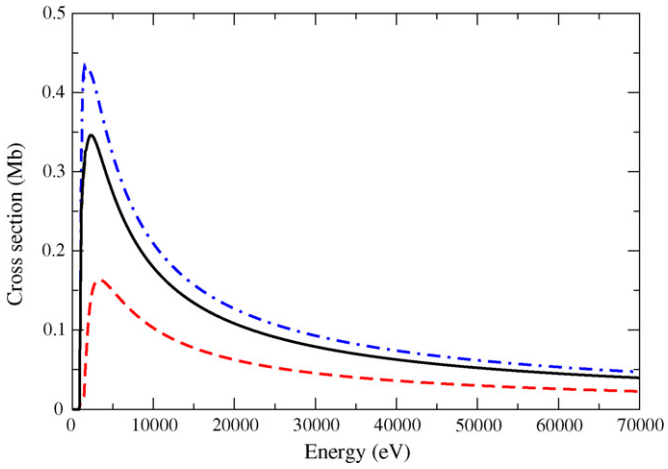

Fig. 2. Electron impact single ionization cross-section for Xe^{25+}. The dashed line shows the total direct ionization cross-section. The dot-dashed lines show the CADW direct ionization plus the CADW excitation-autoionization with unity branching. The solid line shows the CADW direct ionization plus the CADW excitation-autoionization with CADW branching factors.

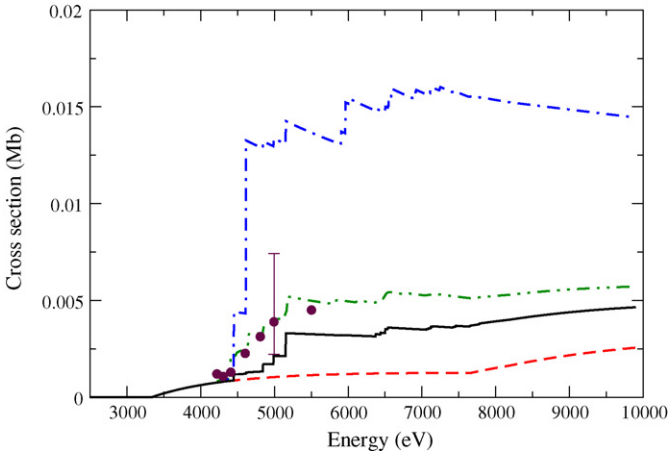

Fig. 3. Electron impact single ionization cross-section for Xe^{43+}. The dashed line shows the total CADW direct ionization cross-section. The dot-dashed line shows the CADW direct ionization plus the CADW excitation-autoionization with unity branching. The solid line shows the total CADW direct ionization plus excitation-autoionization cross-sections with CADW branching. The double-dot dashed line shows the CADW direct ionization plus level-resolved excitation-autoionization with level-resolved branching. The circles show the measurements of Schneider et al. [22].

Table 1
Ground state configurations for Xe ions

Ion stage	Configuration	Single IP (eV)	Direct subshell contributions	Excitation-autoionization contributions
0	[Kr] $4d^{10}5s^25p^6$	12.49	5p,5s,4d*,4p*	5s,4d*,4p*
1	[Kr] $4d^{10}5s^25p^5$	21.73	5p,5s,4d*,4p*	5s,4d*,4p*
2	[Kr] $4d^{10}5s^25p^4$	31.72	5p,5s,4d*,4p*	5s,4d†,4p*
3	[Kr] $4d^{10}5s^25p^3$	42.35	5p,5s,4d*,4p*	5s,4d†,4p*
4	[Kr] $4d^{10}5s^25p^2$	53.58	5p,5s,4d,4p*	5s,4d,4p*
5	[Kr] $4d^{10}5s^25p$	65.33	5p,5s,4d,4p*	5s,4d,4p*
6	[Kr] $4d^{10}5s^2$	90.56	5s,4d,4p*,4s*	4d,4p†,4s*
7	[Kr] $4d^{10}5s$	105.09	5s,4d,4p,4s*	4d,4p,4s†
8	[Kr] $4d^{10}$	180.08	4d,4p,4s,3d*	4p,4s,3d*
9	[Kr] $4d^9$	205.23	4d,4p,4s,3d*	4p,4s,3d*
10	[Kr] $4d^8$	231.17	4d,4p,4s,3d*	4p,4s,3d*
11	[Kr] $4d^7$	257.87	4d,4p,4s,3d*	4p,4s,3d*
12	[Kr] $4d^6$	285.32	4d,4p,4s,3d*	4p,4s,3d*
13	[Kr] $4d^5$	313.49	4d,4p,4s,3d*	4p,4s,3d†
14	[Kr] $4d^4$	342.37	4d,4p,4s,3d*	4p,4s,3d†
15	[Kr] $4d^3$	371.96	4d,4p,4s,3d*	4p,4s,3d†
16	[Kr] $4d^2$	402.24	4d,4p,4s,3d*	4p,4s,3d†
17	[Kr] 4d	433.20	4d,4p,4s,3d*	4p,4s,3d†
18	[Ar] $3d^{10}4s^24p^6$	556.28	4p,4s,3d*,3p*	4s,3d
19	[Ar] $3d^{10}4s^24p^5$	589.18	4p,4s,3d,3p*	4s,3d
20	[Ar] $3d^{10}4s^24p^4$	622.59	4p,4s,3d,3p*	4s,3d
21	[Ar] $3d^{10}4s^24p^3$	656.49	4p,4s,3d,3p*	4s,3d
22	[Ar] $3d^{10}4s^24p^2$	690.88	4p,4s,3d,3p*	4s,3d
23	[Ar] $3d^{10}4s^24p$	725.75	4p,4s,3d,3p*	4s,3d
24	[Ar] $3d^{10}4s^2$	819.22	4s,3d,3p*,3s*	3d,3p
25	[Ar] $3d^{10}4s$	857.42	4s,3d,3p,3s	3d,3p
26	[Ar] $3d^{10}$	1500.89	3d,3p,3s	3p,3s
27	[Ar] $3d^9$	1582.46	3d,3p,3s	3p,3s
28	[Ar] $3d^8$	1665.62	3d,3p,3s	3p,3s
29	[Ar] $3d^7$	1750.36	3d,3p,3s	3p,3s
30	[Ar] $3d^6$	1836.67	3d,3p,3s	3p,3s
31	[Ar] $3d^5$	1924.54	3d,3p,3s	3p,3s
32	[Ar] $3d^4$	2013.98	3d,3p,3s	3p,3s
33	[Ar] $3d^3$	2104.97	3d,3p,3s	3p,3s
34	[Ar] $3d^2$	2197.51	3d,3p,3s	3p,3s
35	[Ar] 3d	2291.60	3d,3p,3s	3p,3s
36	[Ne] $3s^23p^6$	2584.03	3p,3s,2p*	3s,2p†
37	[Ne] $3s^23p^5$	2668.40	3p,3s,2p*	3s,2p†
38	[Ne] $3s^23p^4$	2753.67	3p,3s,2p*	3s,2p†
39	[Ne] $3s^23p^3$	2839.84	3p,3s,2p*	3s,2p†
40	[Ne] $3s^23p^2$	2926.91	3p,3s,2p*	3s,2p†
41	[Ne] $3s^23p$	3014.88	3p,3s,2p*	3s,2p†
42	[Ne] $3s^2$	3245.34	3s,2p*,2s*	2p†,2s†
43	[Ne] 3s	3335.29	3s,2p,2s	2p,2s
44	$1s^22s^22p^6$	7777.36	2p,2s,1s*	2s,1s*
45	$1s^22s^22p^5$	8016.98	2p,2s,1s*	2s,1s*
46	$1s^22s^22p^4$	8259.64	2p,2s,1s*	2s,1s*
47	$1s^22s^22p^3$	8505.37	2p,2s,1s*	2s,1s*
48	$1s^22s^22p^2$	8754.16	2p,2s,1s*	2s,1s*
49	$1s^22s^22p$	9006.03	2p,2s,1s*	2s,1s*
50	$1s^22s^2$	9586.57	2s,1s*	1s*
51	$1s^22s$	9814.99	2s,1s	1s
52	$1s^2$	40302.49	1s	
53	1s	41271.32	1s	

The direct ionization contributions are shown by subshell, as are the subshell excitations included. Star superscripts denote that the transition lies above the double ionization threshold for the ion stage. Dagger superscripts indicate that some autoionizing configurations lie in the single ionization regime and some lie above the double ionization threshold.

Table 2
Ground state configurations for Sn ions

Ion stage	Configuration	Single IP (eV)	Direct subshell contributions	Excitation-autoionization contributions
0	[Kr] $4d^{10}5s^25p^2$	7.08	5p,5s,4d*,4p*	5s,4d*,4p*
1	[Kr] $4d^{10}5s^25p$	14.40	5p,5s,4d,4p*	5s,4d,4p*
2	[Kr] $4d^{10}5s^2$	29.36	5s,4d,4p*,4s*	4d,4p*,4s*
3	[Kr] $4d^{10}5s$	40.07	5s,4d,4p*,4s*	4d,4p†,4s*
4	[Kr] $4d^{10}$	76.51	4d,4p,4s*,3d*	4p,4s†,3d*
5	[Kr] $4d^9$	96.02	4d,4p,4s*,3d*	4p,4s,3d*
6	[Kr] $4d^8$	116.49	4d,4p,4s,3d*	4p,4s,3d*
7	[Kr] $4d^7$	137.83	4d,4p,4s,3d*	4p,4s,3d*
8	[Kr] $4d^6$	160.02	4d,4p,4s,3d*	4p,4s,3d*
9	[Kr] $4d^5$	183.02	4d,4p,4s,3d*	4p,4s,3d*
10	[Kr] $4d^4$	206.79	4d,4p,4s,3d*	4p,4s,3d*
11	[Kr] $4d^3$	231.32	4d,4p,4s,3d*	4p,4s,3d*
12	[Kr] $4d^2$	256.59	4d,4p,4s,3d*	4p,4s,3d†
13	[Kr] 4d	282.58	4d,4p,4s,3d*	4p,4s,3d†
14	[Ar] $3d^{10}4s^24p^6$	383.76	4p,4s,3d*,3p*	4s,3d†
15	[Ar] $3d^{10}4s^24p^5$	412.21	4p,4s,3d*,3p*	4s,3d
16	[Ar] $3d^{10}4s^24p^4$	441.19	4p,4s,3d,3p*	4s,3d
17	[Ar] $3d^{10}4s^24p^3$	470.67	4p,4s,3d,3p*	4s,3d
18	[Ar] $3d^{10}4s^24p^2$	500.66	4p,4s,3d,3p*	4s,3d
19	[Ar] $3d^{10}4s^24p$	531.14	4p,4s,3d,3p*	4s,3d
20	[Ar] $3d^{10}4s^2$	608.55	4s,3d,3p*,3s*	3d,3p
21	[Ar] $3d^{10}4s$	642.24	4s,3d,3p,3s	3d,3p
22	[Ar] $3d^{10}$	1132.71	3d,3p,3s	3p,3s
23	[Ar] $3d^9$	1204.82	3d,3p,3s	3p,3s
24	[Ar] $3d^8$	1278.53	3d,3p,3s	3p,3s
25	[Ar] $3d^7$	1353.84	3d,3p,3s	3p,3s
26	[Ar] $3d^6$	1430.73	3d,3p,3s	3p,3s
27	[Ar] $3d^5$	1509.19	3d,3p,3s	3p,3s
28	[Ar] $3d^4$	1589.23	3d,3p,3s	3p,3s
29	[Ar] $3d^3$	1670.84	3d,3p,3s	3p,3s
30	[Ar] $3d^2$	1754.00	3d,3p,3s	3p,3s
31	[Ar] 3d	1838.71	3d,3p,3s	3p,3s
32	[Ne] $3s^23p^6$	2095.06	3p,3s,2p*	3s,2p†
33	[Ne] $3s^23p^5$	2171.44	3p,3s,2p*	3s,2p†
34	[Ne] $3s^23p^4$	2248.71	3p,3s,2p*	3s,2p†
35	[Ne] $3s^23p^3$	2326.88	3p,3s,2p*	3s,2p†
36	[Ne] $3s^23p^2$	2405.95	3p,3s,2p*	3s,2p†
37	[Ne] $3s^23p$	2485.91	3p,3s,2p*	3s,2p†
38	[Ne] $3s^2$	2682.19	3s,2p*,2s*	2p†,2s†
39	[Ne] 3s	2764.06	3s,2p,2s	2p,2s
40	$1s^22s^22p^6$	6497.57	2p,2s,1s*	2s,1s*
41	$1s^22s^22p^5$	6716.45	2p,2s,1s*	2s,1s*
42	$1s^22s^22p^4$	6938.35	2p,2s,1s*	2s,1s*
43	$1s^22s^22p^3$	7163.27	2p,2s,1s*	2s,1s*
44	$1s^22s^22p^2$	7391.21	2p,2s,1s*	2s,1s*
45	$1s^22s^22p$	7622.18	2p,2s,1s*	2s,1s*
46	$1s^22s^2$	8102.46	2s,1s*	1s*
47	$1s^22s$	8311.60	2s,1s	1s
48	$1s^2$	34287.60	1s	
49	1s	35176.62	1s	

The direct ionization contributions are shown by subshell, as are the subshell excitations included. Star superscripts denote that the transition lies above the double ionization threshold for the ion stage. Dagger superscripts indicate that some autoionizing configurations lie in the single ionization regime and some lie above the double ionization threshold.

tial, indicating a metastable fraction in the experiment. It was shown by Bannister et al. [20] that when account is taken of the metastable fraction, good agreement between experiment and configuration-average distorted-wave theory is achieved. Thus, by Xe^{8+} the configuration-average distorted-wave method is producing good agreement with experimental measurements.

For Xe^{9+} through to Xe^{14+} the excitation-autoionization contribution is small and we expect the configuration-average approach to give accurate results for the direct ionization. The excitation-autoionization contribution increases steadily from Xe^{15+} through to Xe^{25+}. Fig. 2 shows the results for Xe^{25+}. We show results for the excitation-autoionization contribution

with radiative branching of the autoionizing configuration calculated in the configuration-average distorted-wave approach. The decrease in the excitation-autoionization contribution is found to be small and it would be a reasonable approximation to assume that all of the ion stages from Xe^{15+} through to Xe^{25+} have Auger yields of one.

The excitation-autoionization contribution is small for ion stages Xe^{26+} through to Xe^{35+}, with direct ionization from the 3d subshell dominating the total ionization cross-section. The excitation-autoionization contribution for Xe^{36+} through to Xe^{43+} is large and one would expect the Auger yields to be less than one. Fig. 3 shows our results for Xe^{43+}, with radiative branching of the autoionizing configurations included. Experimental measurements are also available for Xe^{43+}[22]. The radiative rates for the autoionizing configurations dominate over the Auger rates and the excitation-autoionization contribution is significantly damped out. The experiment clearly verifies the reduction in the excitation-autoionization contribution. Level-resolved excitation-autoionization calculations were recently performed for this ion[2]. While the configuration-average distorted-wave results are in reasonable agreement with experiment, the level-resolved calculations are clearly an improvement to the configuration-average distorted-wave cross-sections. In both the level-resolved and configuration-average cases the excitation-autoionization contribution is significantly damped out. Thus, we recommend using Auger yields of zero for ion stages Xe^{36+}through to Xe^{42+} and our level-resolved Auger yields for Xe^{43+}. Ion stages above Xe^{43+}have ionization cross-sections dominated by direct ionization, and one would expect the small amount of excitation-autoionization to be completely radiatively damped.

Thus, our current recommendation is that one uses branching ratios of unity for ion stages below Xe^{36+} and branching ratios of zero for ion stages above Xe^{36+}. We are currently working on level-resolved branching ratios to be used for the ion stages from Xe^{36+} to Xe^{42+}, to improve the excitation-autoionization contributions for these ion stages.

3.2. Sn ionization

Results are shown for various ion stages of Sn in Figs. 4–6 . There are no experimental measurements of electron-impact ionization of Sn ions, however results do exist for neutral Sn. Fig. 4 shows the neutral Sn results. The configuration-average distorted-wave results clearly overestimate the peak of the cross-section, as one might expect for distorted-wave results for a neutral system. As one progresses up the isonuclear sequence the excitation-autoionization contribution is significant up to Sn^{21+}. Fig. 5 shows the results for Sn^{21+}, with configuration-average radiative branching of the autoionizing configurations included. For Sn^{21+} radiative branching makes only a small reduction in the excitation-autoionization contribution and it would be a reasonable approximation to use unity Auger yields for ion stages up to Sn^{21+}.

[2] Z. Altun, private communication.

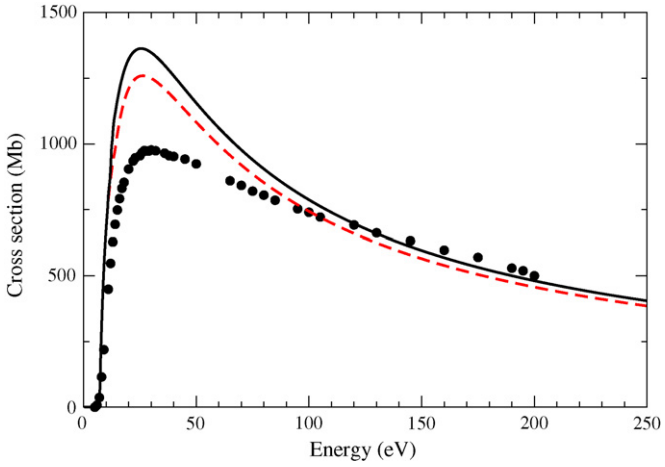

Fig. 4. Electron impact single ionization cross-section for neutral Sn. The dashed line shows the total direct ionization cross-section, the solid line shows the total direct ionization plus excitation-autoionization cross-section. The circles show the measurements of Freund et al. [10].

From ion stages Sn^{22+}through to Sn^{31+} there is very little excitation-autoionization, with direct ionization of the 3d subshell dominating the total ionization cross-section. For ion stages Sn^{32+} through to Sn^{39+} excitation-autoionization becomes significant again. We show results for Sn^{39+} in Fig. 6. It can be seen that the excitation-autoionization contributions is significantly reduced by radiative damping. Thus for ion stages Sn^{32+}through to Sn^{38+}we recommend using Auger yields of zero for the autoionizing configurations. For Sn^{39+} we recommend using our configuration-average Auger yields. Above Sn^{39+} the excitation-autoionization contribution is small, compared with the direct ionization. We are currently working on level-resolved branching ratios for ion stages Sn^{32+} through to Sn^{39+} with a view to improving the available excitation-autoionization contributions for these ion stages.

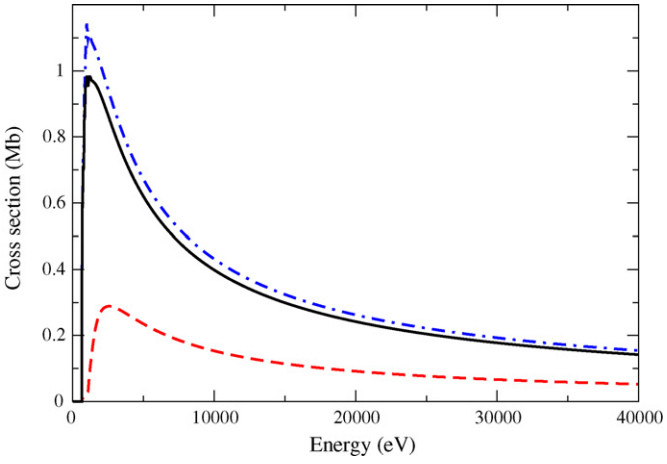

Fig. 5. Electron impact single ionization cross-section for Sn^{21+}. The dashed lines show the direct CADW ionization cross-section. The dot-dashed lines show the CADW direct ionization plus the CADW excitation-autoionization with unity branching. The solid line shows the CADW direct ionization plus the CADW excitation-autoionization with CADW branching factors.

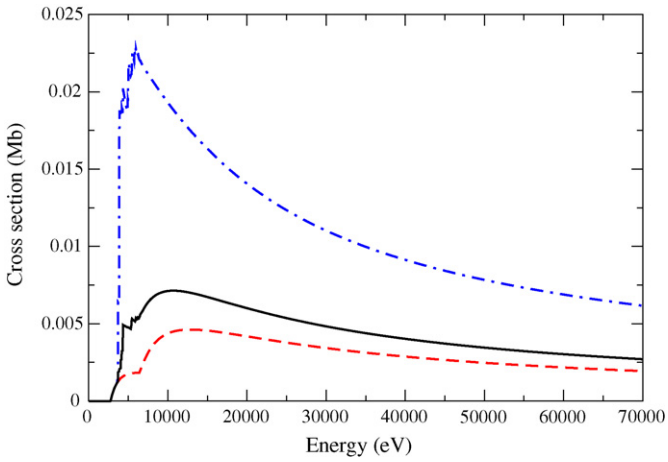

Fig. 6. Electron impact single ionization cross-section for Sn^{39+}. The dashed lines show the direct CADW ionization cross-section. The dot-dashed lines show the CADW direct ionization plus the CADW excitation-autoionization with unity branching. The solid line shows the CADW direct ionization plus the CADW excitation-autoionization with CADW branching factors.

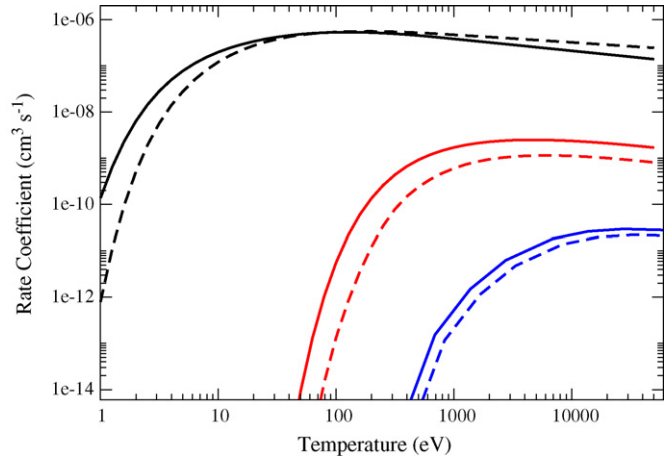

Fig. 7. Plot of selected Sn and Xe total ionization rate coefficients. Results are shown for neutral Sn and Xe (upper most lines), for Cu-like Sn^{21+} and Xe^{25+} (next lowest lines) and for Na-like Sn^{39+} and Xe^{43+} (lowest most lines). The solid lines show the tin rate coefficients and the dashed lines show the xenon rate coefficients.

4. Rate coefficients

For all ion stages of Xe and Sn we produce Maxwellian rate coefficients, for use in modelling codes. We archive the rate coefficients on a 12-point Z-scaled temperature grid. The direct ionization rate coefficients, excitation rate coefficients and branching factors are stored separately. Fig. 7 shows a selection of rate coefficients for both ions. The data is storted in the standard ADAS adf23 data format. The data is made available on the CFADC website [29] and in the ADAS database [30]. We also provide a short fortran code that can be used to read the data.

5. Summary

The electron impact ionzation of all ion stages of Sn and Xe has been calculated, with the results being shown for select ion stages. The direct ionization and excitation cross-sections are calculated using a configuration-average distorted-wave method for all ion stages of both ions. The importance of excitation-autoionization is seen for both elements, and the gradual reduction of the Auger branching ratios as one progresses to higher charge states is also seen. For the lower charge states of Xe, up to Xe^{6+}, the data of Griffin et al. [23] is recommended. It was found that Auger yields of unity are sufficient for Xe through to Xe^{25+} and for Sn through to Sn^{21+}. The Auger yields can be assumed to be zero above Xe^{35+} and Sn^{31+} in their respective iso-nuclear sequences. We include non-zero Auger yields in our Xe^{43+} and Sn^{39+} data files.

Further work is being done on the lower charge states of both elements, to see if the accuracy of the near threshold excitation-autoionization contribution can be improved. Level-resolved excitation-autoionization calculations with radiative branching included are planned for Xe^{36+} through to Xe^{42+} and for Sn^{32+} through to Sn^{39+} to improve the data available for these ion stages. The data for both isonuclear sequences is made available on the CFADC web site [29], and in the ADAS database [30], in a standard format so that it can be used in modelling codes.

Acknowledgements

This work was supported in part by grants from the US Department of Energy. Computational work was carried out at the National Energy Research Scientific Computing Center in Oakland, California. One of the authors (SDL) would like to thank the Oak Ridge National Laboratory for the financial support that funded part of this work.

References

[1] T. Krucken, K. Bergmann, L. Juschkin, R. Lebert, J. Phys. D 37 (2004) 3213.
[2] S. Fujioka, H. Nishimura, K. Nishihara, A. Sasaki, A. Sunahara, T. Okuno, N. Ueda, T. Ando, Y. Tao, Y. Shimada, K. Hashimoto, M. Yamaura, K. Shigemori, M. Nakai, K. Nagai, T. Norimatsu, T. Nishikawa, N. Miyanaga, Y. Izawa, K. Mima, Phys. Rev. Letts 95 (2005) 235004.
[3] M. Arnaud, R. Rothenflug, Astron. Astrophys. Suppl. Ser. 60 (1985) 425.
[4] M.S. Pindzola, D.C. Griffin, N.R. Badnell, H.P. Summers, Nucl. Fusion Suppl. 6 (1996) 117.
[5] K. Dere, Astron. Astrophys. 466 (2007) 771.
[6] S.D. Loch, J. Colgan, M.C. Witthoeft, M.S. Pindzola, C.P. Ballance, D.C. Griffin, M.G. O'Mullane, N.R. Badnell, H.P. Summers, Atomic Data Nucl. Data Tables 92 (2006) 813.
[7] S.D. Loch, M.S. Pindzola, C.P. Ballance, D.C. Griffin, J. Colgan, M.G. O'Mullane, N.R. Badnell, H.P. Summers, Atomic Data Nucl. Data Tables, in press.
[8] S.D. Loch, M.S. Pindzola, C.P. Ballance, D.C. Griffin, D.M. Mitnik, N.R. Badnell, M.G. O'Mullane, H.P. Summers, A.D. Whiteford, Phys. Rev. A 66 (2002) 052708.
[9] S.D. Loch, J.A. Ludlow, M.S. Pindzola, A.D. Whiteford, D.C. Griffin, Phys. Rev. A 72 (2005) 052716.
[10] R.S. Freund, R.C. Wetzel, R.J. Shul, T.R. Hayes, Phys. Rev. A 41 (1990) 3575.
[11] E.J. McGuire, Phys. Rev. A 16 (1977) 62.
[12] R.C. Wetzel, F.A. Baiocchi, T.R. Hayes, R.S. Freund, Phys. Rev. A 35 (1987) 559.

[13] A. Müller, E. Salzborn, R. Frodl, R. Becker, H. Klein, H. Winter, J. Phys. B 13 (1980) 1877.
[14] K.F. Man, A.C.H. Smith, M.F.A. Harrison, J. Phys. B 20 (1987) 5865.
[15] E.W. Bell, N. Djuric, G.H. Dunn, Phys. Rev. A 48 (1993) 4286.
[16] C. Achenbach, A. Muller, E. Salzborn, R. Becker, J. Phys. B 17 (1984) 1405.
[17] K.F. Man, A.C.H. Smith, M.F.A. Harrison, J. Phys. B 26 (1993) 1365.
[18] D.C. Gregory, P.F. Dittner, D.H. Crandall, Phys. Rev. A 27 (1983) 724.
[19] D.C. Gregory, D.H. Crandall, Phys. Rev. A 27 (1983) 2338.
[20] M.E. Bannister, D.W. Mueller, L.J. Wang, M.S. Pindzola, D.C. Griffin, D.C. Gregory, Phys. Rev. A 38 (1988) 38.
[21] M. Stenke, K. Aichele, D. Hathiramani, G. Hofmann, M. Steidl, R. Volpel, E. Salzborn, Nuc. Instru. Meth. Phys. Res. B 98 (1995) 573.
[22] D. Schneider, D. DeWitt, M.W. Clark, R. Schuch, C.L. Cocke, R. Schmieder, K.J. Reed, M.H. Chen, R.E. Marrs, M. Levin, R. Fortner, Phys. Rev. A 42 (1990) 3889.
[23] D.C. Griffin, C. Bottcher, M.S. Pindzola, S.M. Younger, D.C. Gregory, D.H. Crandall, Phys. Rev. A 29 (1984) 1729.
[24] M.S. Pindzola, D.C. Griffin, C. Bottcher, Phys. Rev. A 27 (1983) 2331.
[25] M.S. Pindzola, D.C. Griffin, C. Bottcher, in: F. Brouillard (Ed.), Atomic Processes in Electron–Ion and Ion–Ion Collisions, NATO Advanced Studies Institute 145 B, Plenum Press, New York, 1986, p. 75.
[26] R.D. Cowan, The Theory of Atomic Structure and Spectra, University of California Press, Berkeley, 1981.
[27] M.S. Pindzola, D.C. Griffin, J.H. Macek, Phys. Rev. A 51 (1995) 2186.
[28] A.M. Howald, D.C. Gregory, R.A. Phaneuf, D.H. Crandall, M.S. Pindzola, Phys. Rev. Lett. 56 (1986) 1675.
[29] http://www-cfadc.phy.ornl.gov/data_and_codes/home.html.
[30] H.P. Summers, The ADAS User Manual, version 2.6 http://adas.phys.strath.ac.uk (2004).